Influence of HPT on Photocatalytic CO_2 Conversion

Subjects: Materials Science, Ceramics

Contributor: Saeid Akrami , Tatsumi Ishihara , Masayoshi Fuji , Kaveh Edalati

Severe plastic deformation (SPD) through the high-pressure torsion (HPT) process has been effectively used in recent years to develop novel active catalysts for CO_2 conversion. HPT as an SPD method has been used since 1935 until now for grain refinement and the production of nanostructured materials. In addition to grain refinement, the introduction of various defects, such as vacancies and dislocations, is another feature of HPT, which resulta in the improvement of the functionality of materials proceeded by this method.

functional properties ultrafine-grained (UFG) materials nanostructured materials

1. Introduction

Nowadays, environmental crises, especially global warming caused by CO_2 emission from burning fossil fuels and humankind activities, are considered one of the most significant challenges in the world. Reduction of CO_2 to reactive CO gas or useful components and fuels, such as CH_4 and CH_3OH, using photocatalysts is one of the clean and new strategies, which is developing rapidly [1][2][3]. In photocatalytic CO_2 conversion, excited electrons transfer from the valence band to the conduction band of the photocatalysts by solar irradiation and contribute to the reduction of CO_2 to form desirable products, as shown in **Figure 1**a [3]. To perform these reduction reactions, some thermodynamic and kinetic conditions should be provided. From the viewpoint of thermodynamics, the standard potential of the reduction and oxidation reactions should be between the valence band and the conduction band of the photocatalyst [3][4]. On the other hand, from the kinetic viewpoint, the electrons should absorb the light, transfer to the conduction band, migrate to the surface of the photocatalyst, and take part in the reactions before combining with the holes [3][4]. To satisfy these kinetic and thermodynamic conditions, a photocatalyst should have some features, including high light absorbance, appropriate band structure, low recombination rate of electrons and holes, easy migration of charge carriers, and high surface affinity to adsorb CO_2 with abundant active sites [3][4]. A combination of these thermodynamic and kinetic factors determines the speed of the reactions and the type of final products in photocatalysis.

Semiconductors, such as TiO_2 [5][6][7], g-C_3N_4 [8][9], and $BiVO_4$ [10][11][12], are typical photocatalysts that have been engineered by various strategies to enhance the catalytic efficiency for CO_2 conversion. Doping with impurities, such as nitrogen, phosphorous, copper, and palladium [13][14][15]; defect engineering [16][17]; strain engineering [18][19]; mesoporous structure production [20]; and heterojunction introduction [21][22] are some of the most promising strategies that have been used so far to improve the optical properties and catalytic activity of various photocatalysts. Among these strategies, doping with impurities is the most investigated and feasible method, but

impurities can increase the recombination rate of electrons and holes [13][14][15]. Therefore, finding new strategies to improve the photocatalytic activity and suppress the recombination rate of electrons and holes is a key issue. In this regard, severe plastic deformation (SPD) through the high-pressure torsion (HPT) method, which is mainly used for nanostructuring of metallic materials, has been used as a new tool to develop active photocatalysts for water splitting [23][24][25][26][27][28][29][30], dye degradation [31][32][33][34], and especially CO_2 conversion [35][36][37][38]. This method not only does not increase the recombination rate of electrons and holes but also effectively suppresses it and improves some other optical properties. The SPD method has also been used effectively to synthesize new families of catalysts, such as high-pressure photocatalysts and high-entropy photocatalysts [23][27].

2. Influence of HPT on Photocatalytic CO_2 Conversion

HPT as an SPD method has been used since 1935 until now for grain refinement and the production of nanostructured materials. In addition to grain refinement, the introduction of various defects, such as vacancies and dislocations, is another feature of HPT, which resulta in the improvement of the functionality of materials proceeded by this method [39][40]. In the HPT method, both large shear strain and high pressure (in the range of several gigapascals) are simultaneously utilized to process or synthesize various ranges of materials [39][40]. Strain and pressure are applied to the material (disc or ring shape) using two anvils that rotate with respect to each other, as shown in **Figure 1**b [41]. Due to the high processing pressure in HPT, it is applicable to hard and less ductile materials, such as high-melting temperature metals (hafnium [42], molybdenum [43], and tungsten [44]), amorphous glasses [45][46], silicon-based semiconductors [47][48], and even ultrahard diamond [49][50]. Another advantage of HPT is its capacity to induce ultra-SPD (i.e., shear strains over 1000 for mechanical alloying) [51]. The inducing ultra-SPD [51] together with fast dynamic diffusion [52][53] introduces the HPT method as a unique path to mechanically synthesize new materials even from immiscible systems [54][55]. Due to these unique features of HPT, the method was even used for the process and synthesis of hard and brittle ceramics, but the number of publications on ceramics is quite limited despite the high potential of these materials for various applications [23][24][25][26][27][28][29][30][31][32][33][34][35][36][37][38][56][57][58][59][60][61][62][63][64][65][66][67][68][69][70][71][72][73][74][75][76][77][78][79][80][81]. Published studies regarding ceramics processed or synthesized by HPT are presented in **Table 1**, although there are other classic publications on HPT processing of ceramics mainly by physicists and geologists [40].

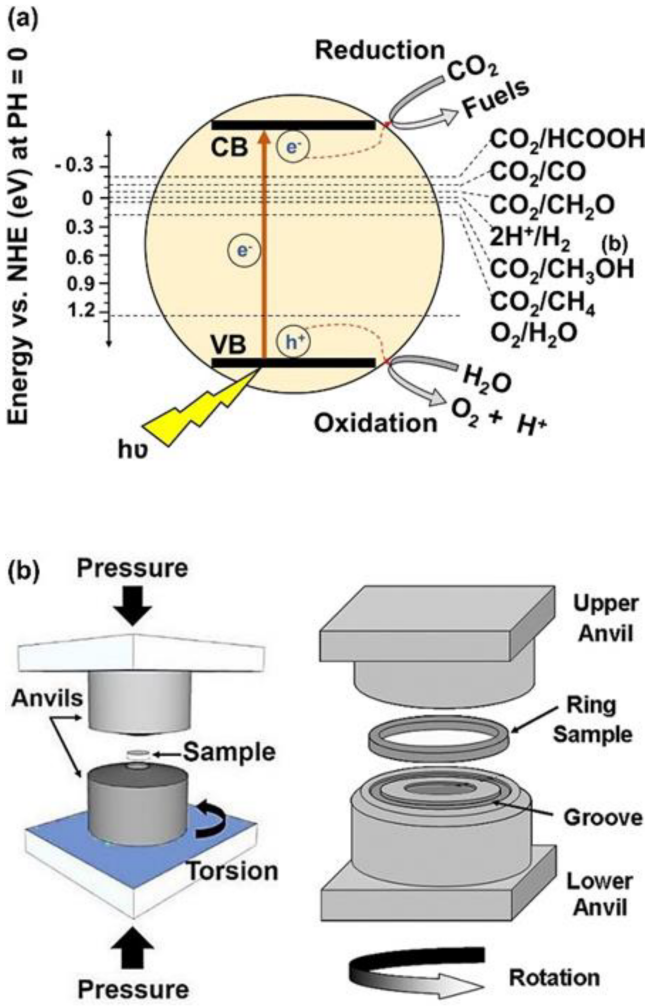

Figure 1. Schematic illustration of (**a**) photocatalytic CO_2 conversion and (**b**) high-pressure torsion [41].

Table 1. Summary of major publications about ceramics treated by high-pressure torsion and their major properties and applications.

Materials	Investigated Properties and Applications	Reference
Various Materials	Impact of pressure and strain on allotropy	Bridgman (1935) [56]
α-Al_2O_3	Microstructure and mechanical properties	Edalati et al. (2010) [57]
ZrO_2	Allotropic phase transformations	Edalati et al. (2011) [58]
CuO	Dielectric properties	Makhnev et al. (2011) [59]
CuO, $Y_3Fe_5O_{12}$, $FeBO_3$	Optical properties and electronic structure	Gizhevskii et al. (2011) [60]
ZrO_2	Phase transformation	Delogu et al. (2012) [61]
Cu_2O, CuO	Middle infrared absorption and X-ray absorption	Mostovshchikova et al.

Materials	Investigated Properties and Applications	Reference
		(2012) [62]
CuO, $Y_3Fe_5O_{12}$, $FeBO_3$	Optical properties	Telegin et al. (2012) [63]
$BaTiO_3$	Optical and dielectric properties	Edalati et al. (2015) [64]
TiO_2-II	Photocatalytic activity for hydrogen production	Razavi-Khosroshahi et al. (2016) [23]
Various Materials	Review on HPT	Edalati et al. (2016) [40]
TiO_2	Plastic strain and phase transformation	Razavi-Khosroshahi et al. (2016) [65]
Y_2O_3	Optical properties	Razavi-Khosroshahi et al. (2016) [66]
$YBa_2Cu_3O_y$	Microstructural investigation	Kuznetsova et al. (2017) [67]
BN	Coupled elastoplasticity and plastic strain-induced phase transformation	Feng et al. (2017) [68]
ZnO	Photocatalytic activity for dye degradation	Razavi-Khosroshahi et al. (2017) [26]
Fe_3O_4	Lithium-ion batteries	Qian et al. (2018) [69]
ZnO	Plastic flow and microstructural instabilities	Qi et al. (2018) [70]
$Fe_{71.2}Cr_{22.7}Mn_{1.3}N_{4.8}$	Microstructural features	Shabashov et al. (2018) [71]
BN	Modeling of plastic flow and strain-induced phase transformation	Feng et al. (2019) [72]
TiO_2-II	Electrocatalysis for hydrogen generation	Edalati et al. (2019) [73]
γ-Al_2O_3	Photocatalytic activity for dye degradation	Edalati et al. (2019) [27]
Various Oxides	Review on HPT of oxides	Edalati et al. (2019) [74]
MgO	Photocatalytic activity for dye degradation	Fujita et al. (2020) [28]
ZrO_2	Photocatalytic activity for hydrogen production	Wang et al. (2020) [26]
SiO_2	Photocatalytic activity for dye degradation	Wang et al. (2020) [34]

Materials	Investigated Properties and Applications	Reference
$CsTaO_3$, $LiTaO_3$	Photocatalytic activity for hydrogen production	Edalati et al. (2020) [24]
GaN-ZnO	Photocatalytic activity for hydrogen production	Edalati et al. (2020) [25]
$Fe_{53.3}Ni_{26.5}B_{20.2}$, $Co_{28.2}Fe_{38.9}Cr_{15.4}Si_{0.3}B_{17.2}$	Microstructure and mechanical properties	Permyakova et al. (2020) [75]
$TiHfZrNbTaO_{11}$	Photocatalytic activity for hydrogen production	Edalati et al. (2020) [27]
TiO_2-ZnO	Photocatalytic activity for hydrogen production	Hidalgo-Jimeneza et al. (2020) [28]
Bi_2O_3	Enhanced photocurrent generation	Fujita et al. (2020) [76]
TiO_2-II	Visible-light photocurrent generation	Wang et al. (2020) [77]
TiO_2-II	Photocatalytic activity for CO_2 conversion	Akrami et al. (2021) [30]
$TiZrHfNbTaO_6N_3$	Photocatalytic activity for hydrogen production	Edalati et al. (2021) [29]
SiO_2, VO_2	Phase transformation	Edalati et al. (2021) [78]
TiO_2	Grain coarsening and phase transformation	Edalati et al. (2021) [79]
ZnO	Bandgap narrowing	Qi et al. (2021) [80]
$BiVO_4$ [35][36][37][38]	Photocatalytic activity for CO_2 conversion	Akrami et al. (2022) [29]
$TiHfZrNbTaO_{11}$	Photocatalytic activity for CO_2 conversion	Akrami et al. (2022) [31] [35][36][37][38]
$TiZrNbTaWO_{12}$	Photocatalytic activity for oxygen production	Edalati et al. (2022) [30]
$TiZrHfNbTaO_6N_3$	Photocatalytic activity for CO_2 conversion	Akrami et al. (2022) [32]

especially ocatalytic bandgap, sites for the HPT ls are not the small n utilized.

However, upscaling the HPT method and increasing the specific surface area by a post-HPT treatment are issues that can be addressed in the future. The improvement of features of photocatalysts by HPT has been achieved using four main strategies, including simultaneous strain and oxygen vacancy engineering, the introduction of high-pressure phases, the formation of defective high-entropy phases, and the production of low-bandgap high-entropy oxynitride phases. The responsibility of each mentioned strategy to improve the photocatalytic CO_2 conversion activity is discussed in detail as follows. It should be noted that all photocatalytic CO_2 conversion experiments on HPT-processed catalysts were performed in an aqueous liquid phase inside a quartz photoreactor with a continuous flow of CO into the liquid phase and $NaHCO_3$ as the sacrificial agent.

2.1. Simultaneous Strain and Oxygen Vacancy Engineering

Oxygen vacancy engineering is an effective method that has been used to improve photocatalytic CO_2 conversion. Oxygen vacancies increase the photocatalytic efficiency by increasing the light absorbance, accelerating the charge carrier separation, and enhancing the surface reactions [35][36]. Oxygen vacancies on the surface of the photocatalysts act as active sites to trap the electrons for various ranges of reduction reactions. It was also observed that oxygen vacancies have a significant role in adsorbing and activating the CO_2 molecules and increasing the local electronic density [35][36].

$BiVO_4$ is one of the common photocatalysts utilized for photocatalytic CO_2 conversion, but it suffers from a high recombination rate of electrons and holes and an inappropriate conduction band position [35]. Different strategies have been used to solve these problems, but in all of them, impurity atoms or a second phase are added to this material [35]. The HPT method was used to solve the problems of $BiVO_4$ for photocatalytic CO_2 conversion by simultaneous engineering of strain and oxygen vacancies without the addition of impurities. $BiVO_4$ was processed by HPT for N = 0.25, 1, and 4 turns to investigate the impact of strain on photocatalytic properties and efficiency. Increasing the lattice strain and decreasing the crystallite size by increasing the HPT turns is shown in **Figure 2**a. The occurrence of lattice strain was also confirmed by Raman peak shift to lower wavenumbers, as shown in **Figure 2**b. It was also observed that the concentration of oxygen vacancies increases in $BiVO_4$ by increasing the applied shear strain. **Figure 2**c illustrates the oxygen vacancy concentration, calculated by X-ray photoelectron spectroscopy (XPS), against the number of HPT turns, confirming that the concentration of vacancies increases by increasing the applied shear strain. Furthermore, strain and vacancy engineering led to an increase in light absorbance (**Figure 2**d) and a slight narrowing of the bandgap from 2.4 eV for the initial powder to 2.1 eV for the sample proceeded by HPT for N = 4 turns [35].

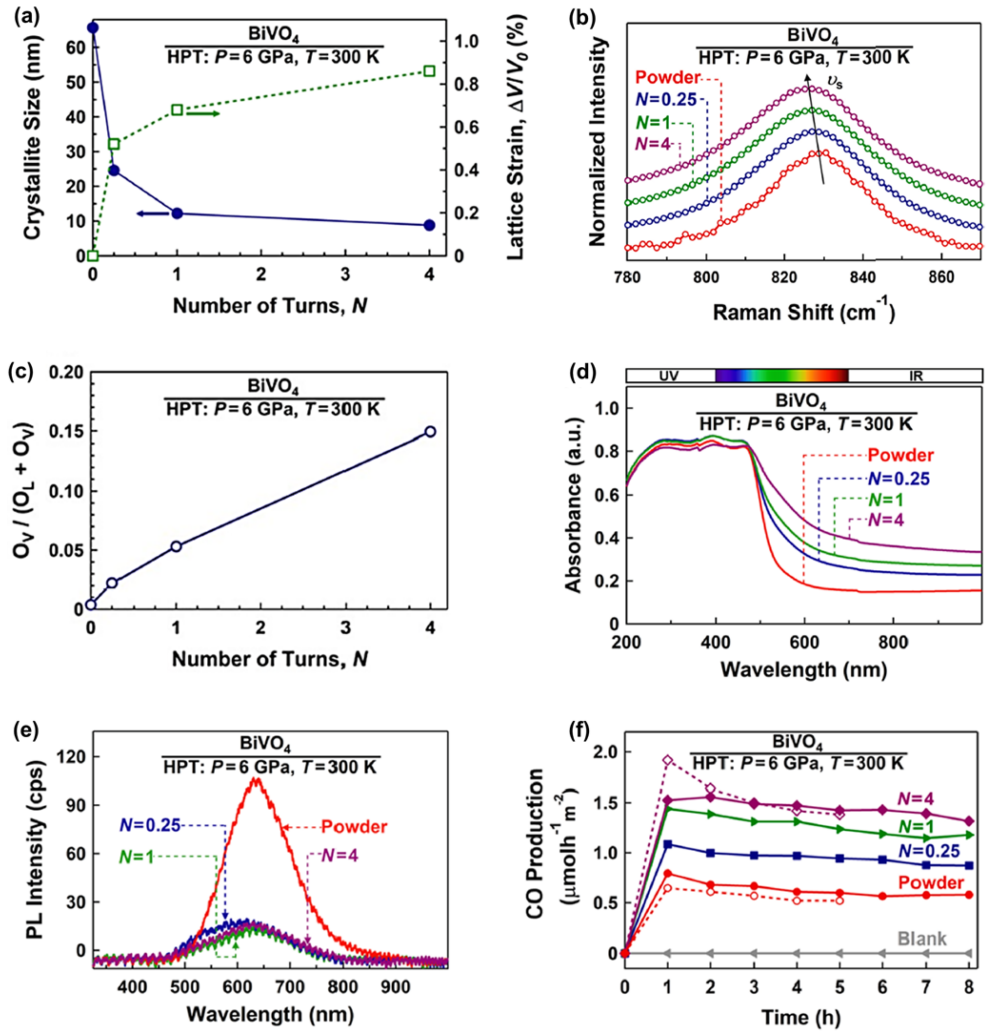

Figure 2. Improvement of light absorbance, suppression of recombination, and enhancement of photocatalytic CO_2 conversion for $BiVO_4$ by simultaneous strain and oxygen vacancy engineering using high-pressure torsion (HPT). (**a**) Crystallite size and volumetric strain versus the number of HPT turns (*N*), (**b**) Raman spectroscopy of initial and HPT-processed samples (inset: the appearance of samples), (**c**) oxygen vacancy concentration versus the number of HPT turns calculated by X-ray photoelectron spectroscopy, (**d**) UV–VIS spectroscopy, (**e**) photoluminescence spectra, and (**f**) photocatalytic CO production rate versus time for initial powder and sample proceeded by HPT for *N* = 0.25, 1, and 4 turns [35].

Simultaneous strain and oxygen vacancy engineering could significantly solve the problem of $BiVO_4$ in terms of the high recombination rate of electrons and holes, as shown in **Figure 2**e. This figure demonstrates that the HPT method decreases the photoluminescence intensity, which is a piece of evidence for the suppression of recombination. Finally, this strategy was successful in improving the photocatalytic activity of $BiVO_4$, as shown in **Figure 2**f. The CO production rate from CO_2 photoreduction was effectively increased by increasing the number of HPT turns. This study was the first successful work that used simultaneous strain and oxygen vacancy engineering to improve the photocatalytic activity of $BiVO_4$ without using impurities, suggesting SPD as a new path to improve the optical and electronic structure of photocatalysts for CO_2 conversion [35].

2.2. Introducing High-Pressure Phases

The formation of high-pressure phases is one of the HPT effects that can occur for some ceramics, such as TiO_2 [65], ZrO_2 [58], ZnO [26], SiO_2 [34], VO_2 [78], Y_2O_3 [66], $BaTiO_3$ [64], Al_2O_3 [27], and BN [68]. It was observed that these high-pressure phases contain defects, such as oxygen vacancies and dislocations, and have nanosized grains, which makes them attractive for photocatalytic applications. TiO_2 with the anatase and rutile crystal structures is one of the most active photocatalysts for CO_2 conversion. As shown in **Figure 3**a, in addition to anatase and rutile, TiO_2 has a high-pressure TiO_2-II (columbite) phase with the orthorhombic structure. Despite many studies on TiO_2 photocatalysts, there was not any research work on photocatalytic CO_2 conversion on the TiO_2-II phase until 2021. Groups of current authors stabilized the TiO_2-II phase by the HPT method and investigated it for photocatalytic CO_2 conversion [36]. To decrease the fraction of oxygen vacancies in the bulk, which can act as recombination centers, an HPT-processed sample was further treated by annealing [36]. The formation of high-pressure TiO_2-II was proved by X-ray diffraction (XRD), Raman spectroscopy, and transmission electron microscopy (TEM). Raman spectra along with the appearance of samples are shown in **Figure 3**b. New Raman peaks at wavenumbers 171, 283, 316, 340, 357, 428, 533, and 572 cm^{-1} correspond to the TiO_2-II phase. The changes in the color of the sample from white to dark green after HPT processing and from dark green to white after annealing indicate that large fractions of oxygen vacancies are formed after HPT processing, while some of them are annihilated after annealing, a fact that was also proved by various characterization techniques [36].

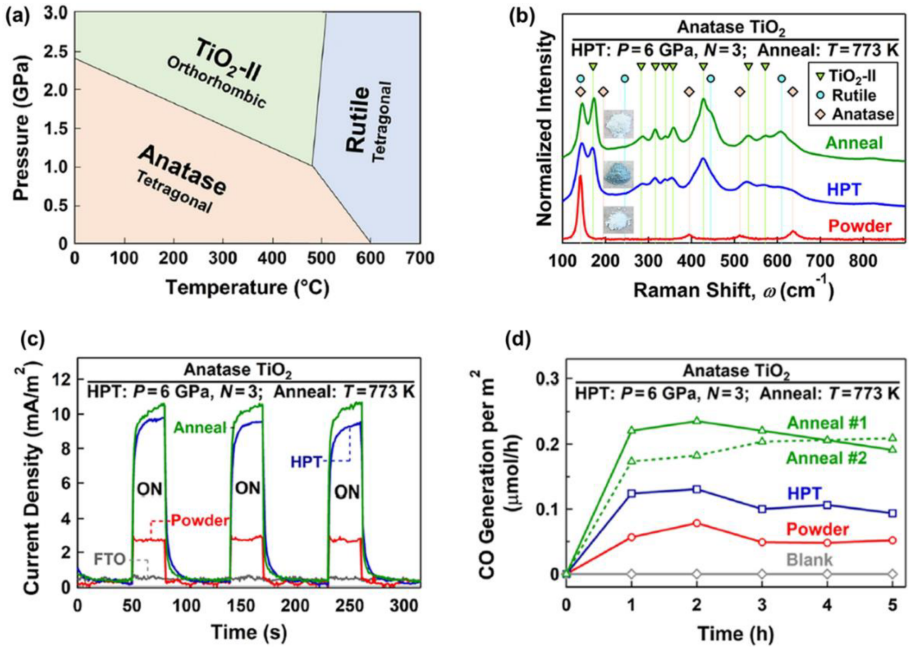

Figure 3. Improved charge carrier migration and photocatalytic CO_2 conversion by introducing the high-pressure TiO_2-II phase. (**a**) Pressure–temperature phase diagram of TiO_2. (**b**) Raman spectra, (**c**) photocurrent spectra, and (**d**) photocatalytic CO production rate versus time for TiO_2 before and after high-pressure torsion processing and after annealing [36].

The light absorbance of the TiO_2-II phase produced by HPT processing was higher, and it had a narrower optical bandgap of 2.5 eV compared with anatase (3 eV), although the bandgap slightly increased to 2.7 eV after annealing [36]. Introducing the high-pressure TiO_2-II phase using HPT suppressed the recombination rate of electrons and holes. It also had a positive impact on photocurrent generation, as shown in **Figure 3**c so that the annealed sample had the highest current density, suggesting the improvement of charge carrier separations by introducing the high-pressure TiO_2-II phase. The potential of this new phase for CO_2 adsorption was measured by attenuated total reflectance Fourier transform infrared (ATR-FTIR) spectroscopy. It was observed that the annealed sample had the highest potential for CO_2 adsorption, which can help with photocatalytic CO_2 conversion. Finally, this new phase showed a higher potential for photocatalytic CO production compared with the anatase phase, as shown in **Figure 3**d. The introduction of the TiO_2-II phase with an optimized fraction of oxygen vacancies significantly improved the activity so that the annealed sample had the highest efficiency for CO_2-to-CO conversion. The formation of anatase–columbite interphases can also contribute to the high activity of the HPT-processed sample by increasing the electron–hole separation and migration. In conclusion, high-pressure phases show great potential to be used as photocatalysts, and SPD can be used to stabilize these high-pressure phases under ambient conditions [36].

2.3. Formation of Defective High-Entropy Phases

Introducing high-entropy ceramics as new materials with five or more principal elements opened a new path in the field of materials science to produce materials with high functionality for various applications [81][82]. High configurational entropy caused by a large number of elements in these materials leads to decreasing the Gibbs free energy and improving the phase stability. High-entropy ceramics have been utilized for various applications, and in many cases, they have shown better efficiencies than conventional materials [81][82]. Li-ion batteries [83], catalysts [84], dielectrics [85], magnetic components [86], thermal barrier coating [87], and so on are some of the applications of these materials. The high potential of high-entropy ceramics for various applications is attributed to their high stability, cocktail effect, lattice distortion, inherent defects, and valence electron distribution [81][82]. Despite the high functionality of these materials, their application for photocatalytic CO_2 conversion was not investigated until a study was conducted by the current authors in 2022 [37].

The HPT method, followed by oxidation, was used to fabricate a defective high-entropy oxide (HEO) with the composition of $TiZrNbHfTaO_{11}$ and dual crystal structure of monoclinic and orthorhombic [37]. The selection of elements for this high-entropy ceramic was conducted by considering the d^0 electronic structure of cations that have shown high potential for photocatalysis. The oxidation states of anionic and cationic elements and their uniform distribution were proved by XPS and energy-dispersive X-ray spectroscopy (EDS), respectively. The microstructure of the oxide is shown in **Figure 4**a using scanning electron microscopy (SEM) and in **Figure 4**b using high-resolution TEM. In addition to a nanocrystalline dual-phase structure, the material exhibited the presence of various defects, such as vacancies and dislocations, as shown in **Figure 4**b. The formation of oxygen vacancies in this material was examined by electron paramagnetic resonance (EPR) spectroscopy. These oxygen vacancies can act as shallow traps between the valence band and the conduction band for easier charge carrier separation, as shown in **Figure 4**c [37].

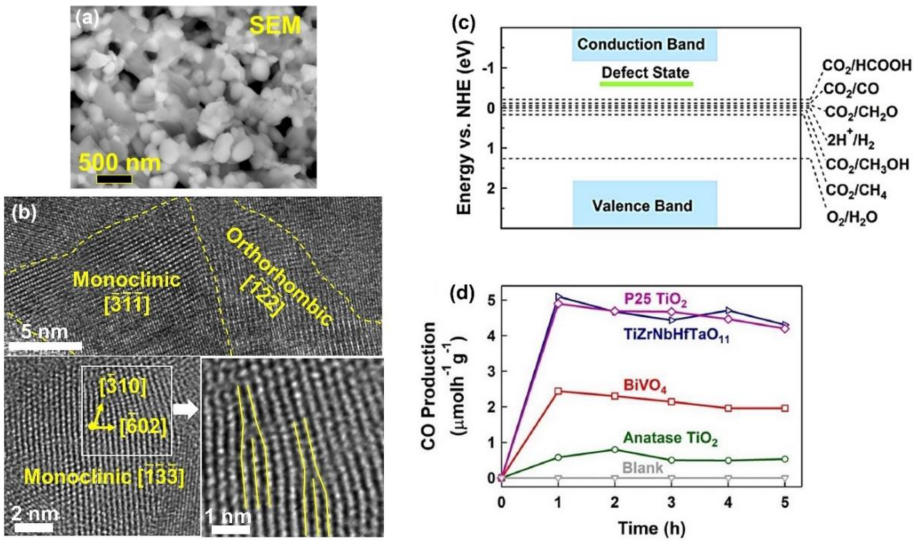

Figure 4. High photocatalytic CO_2 conversion on defective high-entropy oxide $TiZrNbHfTaO_{11}$ synthesized by high-pressure torsion. Microstructure of $TiZrNbHfTaO_{11}$ by (**a**) scanning electron microscopy and (**b**) high-resolution transmission electron microscopy. (**c**) Electronic band structure of $TiZrNbHfTaO_{11}$. (**d**) Photocatalytic CO production rate on $TiZrNbHfTaO_{11}$ versus time compared with P25 TiO_2, $BiVO_4$, and anatase TiO_2 [37].

$TiZrNbHfTaO_{11}$ had a higher light absorbance and lower bandgap compared with the binary oxides, including TiO_2, ZnO, Nb_2O_5, HfO_3, and Ta_2O_5 [37]. This HEO could successfully generate photocurrent, which indicates its potential for easy separation of electrons and holes to improve photocatalytic activity. $TiZrNbHfTaO_{11}$ showed higher activity for photocatalytic CO production compared with $BiVO_4$ and TiO_2 as two typical photocatalysts, as shown in **Figure 4**d. Additionally, it had the same photocatalytic activity as P25 TiO_2 as a benchmark photocatalyst. The high activity of this HEO for photocatalytic CO_2 conversion was attributed to the presence of defects, such as oxygen vacancies and dislocations; interphases; and high light absorbance. This study reported the first application of high-entropy ceramics for photocatalytic CO_2 conversion and introduced a new way to design and synthesize highly efficient high-entropy photocatalysts by SPD processing [37].

2.4. Synthesis of Low-Bandgap High-Entropy Oxynitrides

Metal oxides are the most conventional photocatalysts for CO_2 conversion but suffer from a large bandgap. On the other hand, metal nitrides have a low bandgap but suffer from low stability compared with metal oxides. Metal oxynitrides are rather new materials that can solve the problems of metal oxides and nitrides in terms of large bandgap and low stability, respectively [88]. Although oxynitrides have been used for photocatalytic water splitting in many research works, their application for photocatalytic CO_2 conversion has been limitedly investigated mainly due to their limited chemical stability. The concept of high-entropy materials with high stability is one strategy used to produce high-entropy oxynitrides with low bandgap and high stability for CO_2 photoreduction [38].

A high-entropy oxynitride (HEON) with the composition of $TiZrNbHfTaO_6N_3$ was fabricated by the HPT method, followed by oxidation and nitriding, and its photocatalytic performance was compared with a corresponding HEO $TiZrNbHfTaO_6$ and P25 TiO_2 benchmark photocatalyst [38]. This HEON had dual phases with face-centered cubic

(FCC) and monoclinic structures with uniform distribution of elements. This HEON material had much higher light absorbance compared with P25 TiO_2 and relevant HEO, as shown in **Figure 5**a. It showed a superior low bandgap of 1.6 eV as one of the lowest bandgaps reported in the literature for oxynitride photocatalysts. The improved electronic band structure of this HEON compared with P25 TiO_2 and HEO is shown in **Figure 5**b. The recombination rate of electrons and holes in HEON was low so that its photoluminescence intensity was negligible compared with P25 TiO_2 and HEO (**Figure 5**c). The shape of photocurrent spectra shown in **Figure 5**d also confirmed the low recombination rate of electrons and holes in this HEON compared with the HEO and P25 TiO_2 catalysts. The potential of this HEON for CO_2 adsorption was measured by diffuse reflectance infrared Fourier transform (DRIFT) spectrometry, which showed the higher physical adsorption and chemisorption (in the form of carbonate) of CO_2 on this HEON compared with P25 TiO_2 and HEO (**Figure 5**e).

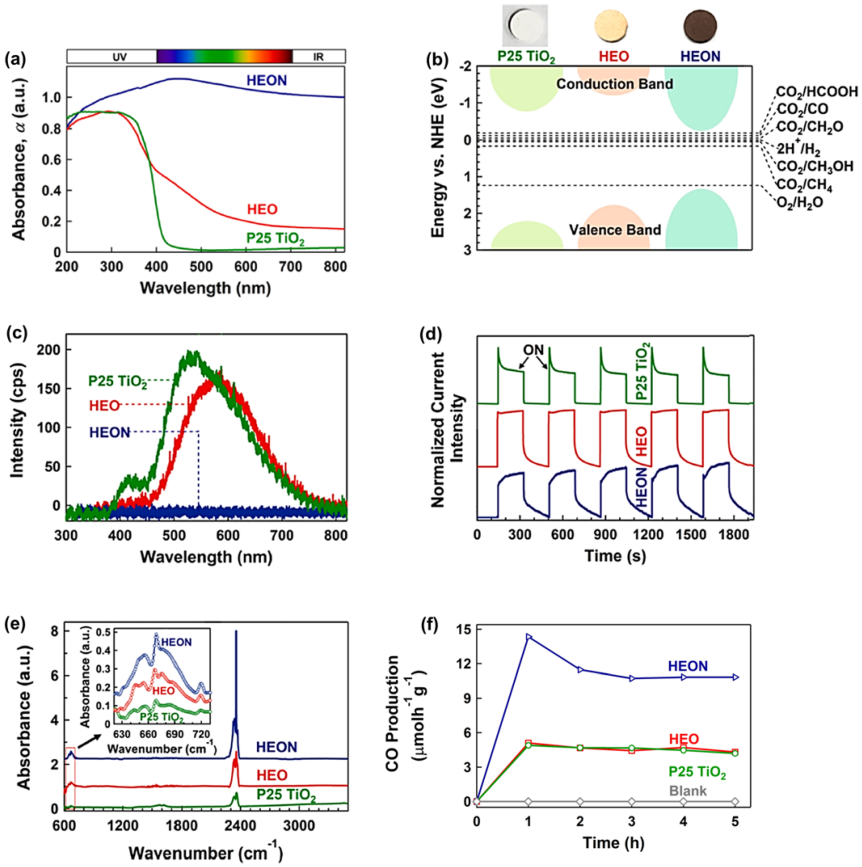

Figure 5. High light absorbance, appropriate band structure, suppressed recombination, significant CO_2 adsorption, and high photocatalytic CO_2 conversion for high-entropy oxynitride (HEON) $TiZrNbHfTaO_6N_3$. (**a**) UV–VIS light absorbance spectra, (**b**) electronic band structure together with the appearance of samples, (**c**) photoluminescence spectra, (**d**) photocurrent density versus time, (**e**) diffuse reflectance infrared Fourier transform spectra (peaks at 665 and 2350 cm^{-1} represent chemisorption and physisorption of CO_2), and (**f**) photocatalytic CO production rate versus time for $TiZrNbHfTaO_6N_3$ compared with P25 TiO_2 and high-entropy oxide (HEO) $TiZrNbHfTaO_{11}$ [38].

This HEON successfully converted CO_2 to CO with extremely high efficiency even compared with the P25 TiO_2 benchmark photocatalyst, as shown in **Figure 5**f. Although HEON could adsorb the light in both visible and infrared regions of light, it could not convert CO_2 in these regions within the detection limits of the gas chromatograph. The stability of HEON was examined by conducting a long-term photocatalytic test for 20 h after storage of the sample in the air for 6 months. The photocatalytic activity of the material was not degraded, and X-ray diffraction analysis confirmed that the crystal structure of HEON did not change after 6-month storage and the long-time photocatalytic reaction. In conclusion, the low-bandgap HEON catalysts synthesized by SPD can be considered a new family of highly efficient photocatalysts for CO_2 conversion [38].

References

1. Forkel, M.; Carvalhais, N.; Rodenbeck, C.; Keeling, R.; Heimann, M.; Thonicke, K.; Zaehle, S.; Reichstein, M. Enhanced seasonal CO2 exchange caused by amplified plant productivity in northern ecosystems. Science 2016, 351, 696–699.
2. Morris, A.J.; Meyer, G.J.; Fujita, E. Molecular approaches to the photocatalytic reduction of carbon dioxide for solar fuels. Acc. Chem. Res. 2009, 42, 1983–1994.
3. Tong, H.; Ouyang, S.; Bi, Y.; Umezawa, N.; Oshikiri, M.; Ye, J. Nano-photocatalytic materials: Possibilities and challenges. Adv. Mater. 2012, 24, 229–251.
4. Li, X.; Yu, J.; Jiang, C. Chapter 1—Principle and surface science of photocatalysis. Interface Sci. Technol. 2020, 31, 1–38.
5. Ola, O.; Maroto-Valer, M.M. Synthesis, characterization and visible light photocatalytic activity of metal based TiO2 monoliths for CO2 reduction. Chem. Eng. J. 2016, 283, 1244–1253.
6. Neatu, S.; Macia-Agullo, J.A.; Concepcion, P.; Garcia, H. Gold-copper nanoalloys supported on TiO2 as photocatalysts for CO2 reduction by water. J. Am. Chem. Soc. 2014, 136, 15969–15976.
7. Kocí, K.; Mateju, K.; Obalova, L.; Krejcikova, S.; Lacny, Z.; Placha, D.; Capek, L.; Hospodkova, A.; Solcova, O. Effect of silver doping on the TiO2 for photocatalytic reduction of CO2. Appl. Catal. B 2010, 96, 239–244.
8. Akhundi, A.; Habibi-Yangjeh, A.; Abitorabi, M.; Pouran, S.R. Review on photocatalytic conversion of carbon dioxide to value-added compounds and renewable fuels by graphitic carbon nitride-based photocatalysts. Catal. Rev. Sci. Eng. 2019, 61, 595–628.
9. Xia, P.; Antonietti, M.; Zhu, B.; Heil, T.; Yu, J.; Cao, S. Designing defective crystalline carbon nitride to enable selective CO2 photoreduction in the gas phase. Adv. Funct. Mater. 2019, 29, 1900093.

10. Wang, K.; Zhang, L.; Su, Y.; Sun, S.; Wang, Q.; Wang, H.; Wang, W. Boosted CO2 photoreduction to methane via Co doping in bismuth vanadate atomic layers. Catal. Sci. Technol. 2018, 8, 3115–3122.
11. Huang, L.; Duan, Z.; Song, Y.; Li, Q.; Chen, L. BiVO4 microplates with oxygen vacancies decorated with metallic Cu and Bi nanoparticles for CO2 photoreduction. ACS Appl. Nano Mater. 2021, 4, 3576–3585.
12. Zhu, Z.; Yang, C.X.; Hwang, Y.T.; Lin, Y.C.; Wu, R.J. Fuel generation through photoreduction of CO2 on novel Cu/BiVO4. Mater. Res. Bull. 2020, 130, 110955.
13. Lee, G.J.; Anandan, S.; Masten, S.J.; Wu, J.J. Photocatalytic hydrogen evolution from water splitting using Cu doped ZnS microspheres under visible light irradiation. Renew. Energy 2016, 89, 18–26.
14. Liu, B.; Ye, L.; Wang, R.; Yang, J.; Zhang, Y.; Guan, R.; Tian, L.; Chen, X. Phosphorus-doped graphitic carbon nitride nanotubes with amino-rich surface for efficient CO2 capture, enhanced photocatalytic activity, and product selectivity. ACS Appl. Mater. Interfaces 2018, 10, 4001–4009.
15. Kuvarega, A.T.; Krause, R.W.M.; Mamba, B.B. Nitrogen/palladium-codoped TiO2 for efficient visible light photocatalytic dye degradation. J. Phys. Chem. C 2011, 115, 22110–22120.
16. Bai, S.; Zhang, N.; Gao, C.; Xiong, Y. Defect engineering in photocatalytic materials. Nano Energy 2018, 53, 293–336.
17. Di, J.; Zhu, C.; Ji, M.; Duan, M.; Long, R.; Yan, C.; Gu, K.; Xiong, J.; She, Y.; Xia, J.; et al. Defect-rich Bi12O17Cl2 nanotubes self-accelerating charge separation for boosting photocatalytic CO2 reduction. Angew. Chem. 2018, 57, 14847–14851.
18. Cai, X.; Wang, F.; Wang, R.; Xi, Y.; Wang, A.; Wang, J.; Teng, B.; Baiy, S. Synergism of surface strain and interfacial polarization on core-shell cocatalysts for highly efficient photocatalytic CO2 reduction over TiO2. J. Mater. Chem. A 2020, 8, 7350–7359.
19. Liu, Z.; Menendez, C.; Shenoy, J.; Hart, J.N.; Sorrell, C.C.; Cazorl, C. Strain engineering of oxide thin films for photocatalytic applications. Nano Energy 2020, 72, 104732.
20. Li, Y.; Wang, W.N.; Zhan, Z.; Woo, M.H.; Wu, C.Y.; Biswas, P. Photocatalytic reduction of CO2 with H2O on mesoporous silica supported Cu/TiO2 catalysts. Appl. Catal. B 2010, 100, 386–392.
21. Cao, S.; Shen, B.; Tong, T.; Fu, J.; Yu, J. 2D/2D heterojunction of ultrathin MXene/ Bi2WO6 nanosheets for improved photocatalytic CO2 reduction. Adv. Funct. Mater. 2018, 28, 1800136.
22. Li, J.; Shao, W.; Geng, M.; Wan, S.; Ou, M.; Chen, Y. Combined Schottky junction and doping effect in CdxZn1-x/BiVO4 Z-Scheme photocatalyst with boosted carriers charge separation for CO2 reduction by H2O. J. Colloid Interface Sci. 2022, 606, 1469–1476.

23. Razavi-Khosroshahi, H.; Edalati, K.; Hirayama, M.; Emami, H.; Arita, M.; Yamauchi, M.; Hagiwara, H.; Ida, S.; Ishihara, T.; Akiba, E.; et al. Visible- light-driven photocatalytic hydrogen generation on nanosized TiO2-II stabilized by high-pressure torsion. ACS Catal. 2016, 6, 5103–5107.
24. Edalati, K.; Fujiwara, K.; Takechi, S.; Wang, Q.; Arita, M.; Watanabe, M.; Sauvage, X.; Ishihara, T.; Horita, Z. Improved photocatalytic hydrogen evolution on tantalate perovskites CsTaO3 and LiTaO3 by strain-induced vacancies. ACS Appl. Energy Mater. 2020, 3, 1710–1718.
25. Edalati, K.; Uehiro, R.; Takechi, S.; Wang, Q.; Arita, M.; Watanabe, M.; Ishihara, T.; Horita, Z. Enhanced photocatalytic hydrogen production on GaN-ZnO oxynitride by introduction of strain-induced nitrogen vacancy complexes. Acta Mater. 2020, 185, 149–156.
26. Wang, Q.; Edalati, K.; Koganemaru, Y.; Nakamura, S.; Watanabe, M.; Ishihara, T.; Horita, Z. Photocatalytic hydrogen generation on low-bandgap black zirconia (ZrO2) produced by high-pressure torsion. J. Mater. Chem. A 2020, 8, 3643–3650.
27. Edalati, P.; Wang, Q.; Razavi-Khosroshahi, H.; Fuji, M.; Ishihara, T.; Edalati, K. Photocatalytic hydrogen evolution on a high entropy oxide. J. Mater. Chem. A 2020, 8, 3814–3821.
28. Hidalgo-Jimeneza, J.; Wang, Q.; Edalatib, K.; Cubero-Sesína, J.M.; Razavi-Khosroshahid, H.; Ikomac, Y.; Gutiérrez-Fallase, D.; Dittel-Mezaa, F.A.; Rodríguez-Rufinoa, J.C.; Fujid, M.; et al. Phase transformations, vacancy formation and variations of optical and photocatalytic properties in TiO2-ZnO composites by high pressure torsion. Int. J. Plast. 2020, 124, 170–185.
29. Edalati, P.; Shen, X.F.; Watanabe, M.; Ishihara, T.; Arita, M.; Fuji, M.; Edalati, K. High-entropy oxynitride as a low-bandgap and stable photocatalyst for hydrogen production. J. Mater. Chem. A 2021, 9, 15076–15086.
30. Edalati, P.; Itagoe, Y.; Ishihara, H.; Ishihara, T.; Emami, H.; Arita, M.; Fuji, M.; Edalati, K. Visible-light photocatalytic oxygen production on a high-entropy oxide by multiple-heterojunction introduction. J. Photochem. Photobiol. A 2022, 433, 114167.
31. Razavi-Khosroshahi, H.; Edalati, K.; Wu, J.; Nakashima, Y.; Arita, M.; Ikoma, Y.; Sadakiyo, M.; Inagaki, Y.; Staykov, A.; Yamauchi, M.; et al. High-pressure zinc oxide phase as visible-light-active photocatalyst with narrow band gap. J. Mater. Chem. A 2017, 5, 20298–20303.
32. Edalati, K.; Fujita, I.; Takechi, S.; Nakashima, Y.; Kumano, K.; Razavi-Khosroshahi, H.; Arita, M.; Watanabe, M.; Sauvage, X.; Akbay, T.; et al. Photocatalytic activity of aluminum oxide by oxygen vacancy generation using high-pressure torsion straining. Scr. Mater. 2019, 173, 120–124.
33. Fujita, I.; Edalati, K.; Wang, Q.; Arita, M.; Watanabe, M.; Munetoh, S.; Ishihara, T.; Horita, Z. High-pressure torsion to induce oxygen vacancies in nanocrystals of magnesium oxide: Enhanced light absorbance, photocatalysis and significance in geology. Materialia 2020, 11, 100670.
34. Wang, Q.; Edalati, K.; Fujita, I.; Watanabe, M.; Ishihara, T.; Horita, Z. High-pressure torsion of SiO2 quartz sand: Phase transformation, optical properties, and significance in geology. J. Am.

Ceram. Soc. 2020, 103, 6594–6602.

35. Akrami, S.; Murakami, Y.; Watanabe, M.; Ishihara, T.; Arita, M.; Guo, Q.; Fuji, M.; Edalati, K. Enhanced CO2 conversion on highly-strained and oxygen-deficient BiVO4 photocatalyst. Chem. Eng. J. 2022, 442, 136209.
36. Akrami, S.; Watanabe, M.; Ling, T.H.; Ishihara, T.; Arita, M.; Fuji, M.; Edalati, K. High pressure TiO2-II polymorph as an active photocatalyst for CO2 to CO conversion. Appl. Catal. B 2021, 298, 120566.
37. Akrami, S.; Murakami, Y.; Watanabe, M.; Ishihara, T.; Arita, M.; Fuji, M.; Edalati, K. Defective high-entropy oxide photocatalyst with high activity for CO2 conversion. Appl. Catal. B 2022, 303, 120896.
38. Akrami, S.; Edalati, P.; Shundo, Y.; Watanabe, M.; Ishihara, T.; Fuji, M.; Edalati, K. Significant CO2 photoreduction on a high-entropy oxynitride. Chem. Eng. J. 2022, 449, 137800.
39. Edalati, K.; Bachmaier, A.; Beloshenko, V.A.; Beygelzimer, Y.; Blank, V.D.; Botta, W.J.; Bryła, K.; Čížek, J.; Divinski, S.; Enikeev, N.A.; et al. Nanomaterials by severe plastic deformation: Review of historical developments and recent advances. Mater. Res. Lett. 2022, 10, 163–256.
40. Edalati, K.; Horita, Z. A review on high-pressure torsion (HPT) from 1935 to 1988. Mater. Sci. Eng. A 2016, 652, 325–352.
41. Edalati, K.; Horita, Z. Scaling-up of high pressure torsion using ring shape. Mater. Trans. 2009, 50, 92–95.
42. Edalati, K.; Horita, Z.; Mine, Y. High-pressure torsion of hafnium. Mater. Sci. Eng. A 2010, 527, 2136–2141.
43. Lee, S.; Edalati, K.; Horita, Z. Microstructures and mechanical properties of pure V and Mo processed by high-pressure torsion. Mater. Trans. 2010, 51, 1072–1079.
44. Chen, L.; Ping, L.; Ye, T.; Lingfeng, L.; Kemin, X.; Meng, Z. Observations on the ductility and thermostability of tungsten processed from micropowder by improved high-pressure torsion. Rare Met. Mater. Eng. 2016, 45, 3089–3094.
45. Edalati, K.; Yokoyama, Y.; Horita, Z. High-pressure torsion of machining chips and bulk discs of amorphous Zr50Cu30Al10Ni10. Mater. Trans. 2010, 51, 23–26.
46. Wang, Y.B.; Qu, D.D.; Wang, X.H.; Cao, Y.; Liao, X.Z.; Kawasaki, M.; Ringer, S.P.; Shan, Z.W.; Langdon, T.G.; Shen, J. Introducing a strain-hardening capability to improve the ductility of bulk metallic glasses via severe plastic deformation. Acta Mater. 2012, 60, 253–260.
47. Edalati, K.; Horita, Z. Correlations between hardness and atomic bond parameters of pure metals and semi-metals after processing by high-pressure torsion. Scr. Mater. 2011, 64, 161–164.

48. Ikoma, Y.; Hayano, K.; Edalati, K.; Saito, K.; Guo, Q.; Horita, Z. Phase transformation and nanograin refinement of silicon by processing through high-pressure torsion. Appl. Phys. Lett. 2012, 101, 121908.
49. Blank, V.D.; Churkin, V.D.; Kulnitskiy, B.A.; Perezhogin, I.A.; Kirichenko, A.N.; Erohin, S.V.; Sorokin, P.B.; Popov, M.Y. Pressure-induced transformation of graphite and diamond to onions. Crystals 2018, 8, 68.
50. Gao, Y.; Ma, Y.; An, Q.; Levitas, V.I.; Zhang, Y.; Feng, B.; Chaudhuri, J.; Goddard, W.A. III: Shear driven formation of nano-diamonds at sub-gigapascals and 300 K. Carbon 2019, 146, 364–368.
51. Edalati, K.; Uehiro, R.; Fujiwara, K.; Ikeda, Y.; Li, H.W.; Sauvage, X.; Valiev, R.Z.; Akiba, E.; Tanaka, I.; Horita, Z. Ultra-severe plastic deformation: Evolution of microstructure, phase transformation and hardness in immiscible magnesium-based systems. Mater. Sci. Eng. A 2017, 701, 158–166.
52. Oberdorfer, B.; Lorenzoni, B.; Unger, K.; Sprengel, W.; Zehetbauer, M.; Pippan, R.; Wurschum, R. Absolute concentration of free volume-type defects in ultrafine-grained Fe prepared by high-pressure torsion. Scr. Mater. 2010, 63, 452–455.
53. Straumal, B.B.; Mazilkin, A.A.; Baretzky, B.; Schütz, G.; Rabkin, E.; Valiev, R.Z. Accelerated diffusion and phase transformations in Co-Cu alloys driven by the severe plastic deformation. Mater. Trans. 2012, 53, 63–71.
54. Edalati, K.; Emami, H.; Staykov, A.; Smith, D.J.; Akiba, E.; Horita, Z. Formation of metastable phases in magnesium-titanium system by high-pressure torsion and their hydrogen storage performance. Acta Mater. 2015, 50, 150–156.
55. Kormout, K.S.; Pippan, R.; Bachmaier, A. Deformation-induced supersaturation in immiscible material systems during high-pressure torsion. Adv. Eng. Mater. 2017, 19, 1600675.
56. Bridgman, P.W. Effects of high shearing stress combined with high hydrostatic pressure. Phys. Rev. 1935, 48, 825–847.
57. Edalati, K.; Horita, Z. Application of high-pressure torsion for consolidation of ceramic Powders. Scr. Mater. 2010, 63, 174–177.
58. Edalati, K.; Toh, S.; Ikomaa, Y.; Horita, Z. Plastic deformation and allotropic phase transformations in zirconia ceramics during high-pressure torsion. Scr. Mater. 2011, 65, 974–977.
59. Makhnev, A.A.; Nomerovannaya, L.V.; Gizhevskii, B.A.; Naumov, S.V.; Kostromitin, N.V. Effect of redistribution of the optical spectral weight in CuO nanostructured ceramics. Solid State Phenom. 2011, 168–169, 285–288.
60. Gizhevskii, B.A.; Sukhorukov, Y.P.; Nomerovannaya, L.V.; Makhnev, A.A.; Ponosov, Y.S.; Telegin, A.V.; Mostovshchikov, E.V. Features of optical properties and the electronic structure of

nanostructured oxides of 3D-Metals. Solid State Phenom. 2011, 168–169, 317–320.

61. Delogu, F. Are processing conditions similar in ball milling and high-pressure torsion? The case of the tetragonal-to-monoclinic phase transition in ZrO2 powders. Scr. Mater. 2012, 67, 340–343.
62. Mostovshchikova, E.V.; Gizhevskii, B.A.; Loshkareva, N.N.; Galakhov, V.R.; Naumov, S.V.; Ponosov, Y.S.; Ovechkina, N.A.; Kostromitina, N.V.; Buling, A.; Neumann, M. Infrared and X-ray absorption spectra of Cu2O and CuO nanoceramics. Solid State Phenom. 2012, 190, 683–686.
63. Telegin, A.V.; Gizhevskii, B.A.; Nomerovannaya, L.V.; Makhnev, A.A. The optical and magneto-optical properties of nanostructured oxides of 3d-metals. J. Supercond. Nov. Magn. 2012, 25, 2683–2686.
64. Edalati, K.; Arimura, M.; Ikoma, Y.; Daio, T.; Miyata, M.; Smith, D.J.; Horita, Z. Plastic deformation of BaTiO3 ceramics by high-pressure torsion and changes in phase transformations, optical and dielectric properties. Mater. Res. Lett. 2015, 3, 216–221.
65. Razavi-Khosroshahi, H.; Edalati, K.; Arita, M.; Horita, Z.; Fuji, M. Plastic strain and grain size effect on high-pressure phase transformations in nanostructured TiO2 ceramics. Scr. Mater. 2016, 124, 59–62.
66. Razavi-Khosroshahi, H.; Edalati, K.; Emami, H.; Akiba, E.; Horita, Z.; Fuji, M. Optical properties of nanocrystalline monoclinic Y2O3 stabilized by grain size and plastic strain effects via high-pressure torsion. Inorg. Chem. 2017, 56, 2576–2580.
67. Kuznetsova, E.I.; Degtyarev, M.V.; Zyuzeva, N.A.; Bobylev, I.B.; Pilyugin, V.P. Microstructure of YBa2Cu3Oy subjected to severe plastic deformation by high pressure torsion. Phys. Met. Metallogr. 2017, 118, 815–823.
68. Feng, B.; Levitas, V.I. Coupled elastoplasticity and plastic strain-induced phase transformation under high pressure and large strains: Formulation and application to BN sample compressed in a diamond anvil cell. Int. J. Plast. 2017, 96, 156–181.
69. Qian, C.; He, Z.; Liang, C.; Ji, W. New in situ synthesis method for Fe3O4/flake graphite nanosheet composite structure and its application in anode materials of lithium-ion batteries. J. Nanomater. 2018, 2018, 2417949.
70. Qi, Y.; Kosinova, A.; Kilmametov, A.R.; Straumal, B.B.; Rabkin, E. Plastic flow and microstructural instabilities during high-pressure torsion of Cu/ZnO composites. Mater. Charact. 2018, 145, 389–401.
71. Shabashov, V.A.; Makarov, A.V.; Kozlov, K.A.; Sagaradze, V.V.; Zamatovskii, A.E.; Volkova, E.G.; Luchko, S.N. Deformation-induced dissolution and precipitation of nitrides in austenite and ferrite of a high-nitrogen stainless steel. Phys. Met. Metallogr. 2018, 119, 193–204.

72. Feng, B.; Levitas, V.I.; Li, W. FEM modeling of plastic flow and strain-induced phase transformation in BN under high pressure and large shear in a rotational diamond anvil cell. Int. J. Plast. 2019, 113, 236–254.
73. Edalati, K.; Wang, Q.; Eguchi, H.; Razavi-Khosroshahi, H.; Emami, H.; Yamauchi, M.; Fuji, M.; Horita, Z. Impact of TiO2-II phase stabilized in anatase matrix by high-pressure torsion on electrocatalytic hydrogen production. Mater. Res. Lett. 2019, 7, 334–339.
74. Edalati, K. Review on recent advancements in severe plastic deformation of oxides by high-pressure torsion (HPT). Adv. Eng. Mater. 2019, 21, 1800272.
75. Permyakova, I.; Glezer, A. Amorphous-nanocrystalline composites prepared by high-pressure torsion. Metals 2020, 10, 511.
76. Fujita, I.; Edalati, P.; Wang, Q.; Watanabe, M.; Arita, M.; Munetoh, S.; Ishihara, T.; Edalati, K. Novel black bismuth oxide (Bi2O3) with enhanced photocurrent generation, produced by high-pressure torsion straining. Scr. Mater. 2020, 187, 366–370.
77. Wang, Q.; Watanabe, M.; Edalati, K. Visible-light photocurrent in nanostructured high-pressure TiO2-II (Columbite) phase. J. Phys. Chem. C 2020, 124, 13930–13935.
78. Edalati, K.; Fujita, I.; Sauvage, X.; Arita, M.; Horita, Z. Microstructure and phase transformations of silica glass and vanadium oxide by severe plastic deformation via high-pressure torsion straining. J. Alloys Compd. 2019, 779, 394–398.
79. Edalati, K.; Wang, Q.; Razavi-Khosroshahi, H.; Emami, H.; Fuji, M.; Horita, Z. Low-temperature anatase-to-rutile phase transformation and unusual grain coarsening in titanium oxide nanopowders by high-pressure torsion straining. Scr. Mater. 2019, 162, 341–344.
80. Qi, Y.; Kauffmann, Y.; Kosinova, A.; Kilmametov, A.R.; Straumal, B.B.; Rabkin, E. Gradient bandgap narrowing in severely deformed ZnO nanoparticles. Matter. Res. Lett. 2021, 9, 58–64.
81. Akrami, S.; Edalati, P.; Edalati, K.; Fuji, M. High-entropy ceramics: A review of principles, production and applications. Mater. Sci. Eng. R 2021, 146, 100644.
82. Oses, C.; Toher, C.; Curtarolo, S. High-entropy ceramics. Nat. Rev. Mater. 2020, 5, 295–309.
83. Sarkar, A.; Velasco, L.; Wang, D.; Wang, Q.; Talasila, G.; de Biasi, L.; Kübel, C.; Brezesinski, T.; Bhattacharya, S.S.; Hahn, H.; et al. High entropy oxides for reversible energy storage. Nat. Commun. 2018, 9, 3400.
84. Chen, H.; Lin, W.; Zhang, Z.; Jie, K.; Mullins, D.R.; Sang, X.; Yang, S.Z.; Jafta, C.J.; Bridges, C.A.; Hu, X. Mechanochemical synthesis of high entropy oxide materials under ambient conditions: Dispersion of catalysts via entropy maximization. ACS, Mater. Lett. 2019, 1, 83–88.
85. Radon, A.; Hawełek, D.; Łukowiec, J.; Kubacki, P.; Włodarczyk, P. Dielectric and electromagnetic interference shielding properties of high entropy (Zn, Fe, Ni, Mg, Cd)Fe2O4 ferrite. Sci. Rep.

2019, 9, 20078.

86. Witte, R.; Sarkar, A.; Kruk, R.; Eggert, B.; Brand, R.A.; Wende, H.; Hahn, H. High entropy oxides: An emerging prospect for magnetic rare-earth transition metal perovskites. Phys. Rev. Mater. 2019, 3, 034406.
87. Wright, A.J.; Huang, C.; Walock, M.J.; Ghoshal, A.; Murugan, M.; Luo, J. Sand corrosion, thermal expansion, and ablation of medium-and high-entropy compositionally complex fluorite oxides. J. Am. Ceram. Soc. 2021, 104, 448–462.
88. Takata, T.; Pan, C.; Domen, K. Recent progress in oxynitride photocatalysts for visible-light-driven water splitting. Sci. Technol. Adv. Mater. 2015, 16, 033506.